ARTICLE

Check for updates

Defect engineering of silicon with ion pulses from laser acceleration

Walid Redjem[1], Ariel J. Amsellem [2], Frances I. Allen [3,4], Gabriele Benndorf[5], Jianhui Bin [2,11], Stepan Bulanov[2], Eric Esarey[2], Leonard C. Feldman[6], Javier Ferrer Fernandez [7,8], Javier Garcia Lopez [7,8], Laura Geulig [2,12], Cameron R. Geddes[2], Hussein Hijazi[6], Qing Ji[2], Vsevolod Ivanov [2,9], Boubacar Kanté [1,2], Anthony Gonsalves[2], Jan Meijer [5], Kei Nakamura [2], Arun Persaud [2], Ian Pong [2], Lieselotte Obst-Huebl [2], Peter A. Seidl [2], Jacopo Simoni[9], Carl Schroeder[2,10], Sven Steinke[2,13], Liang Z. Tan [9], Ralf Wunderlich[5], Brian Wynne [2] & Thomas Schenkel [2✉]

Defect engineering is foundational to classical electronic device development and for emerging quantum devices. Here, we report on defect engineering of silicon with ion pulses from a laser accelerator in the laser intensity range of 10^{19} W cm^{-2} and ion flux levels of up to 10^{22} ions cm^{-2} s^{-1}, about five orders of magnitude higher than conventional ion implanters. Low energy ions from plasma expansion of the laser-foil target are implanted near the surface and then diffuse into silicon samples locally pre-heated by high energy ions from the same laser-ion pulse. Silicon crystals exfoliate in the areas of highest energy deposition. Color centers, predominantly W and G-centers, form directly in response to ion pulses without a subsequent annealing step. We find that the linewidth of G-centers increases with high ion flux faster than the linewidth of W-centers, consistent with density functional theory calculations of their electronic structure. Intense ion pulses from a laser-accelerator drive materials far from equilibrium and enable direct local defect engineering and high flux doping of semiconductors.

[1] Department of Electrical Engineering and Computer Science, University of California, Berkeley, CA 94720, USA. [2] Accelerator Technology and Applied Physics Division, Lawrence Berkeley National Laboratory, Berkeley, CA 94720, USA. [3] Department of Materials Science and Engineering, University of California, Berkeley, CA 94720, USA. [4] California Institute for Quantitative Biosciences, University of California, Berkeley, CA 94720, USA. [5] Felix Bloch Institute for Solid State Physics, University Leipzig, Linnéstr. 5, D-04103 Leipzig, Germany. [6] Rutgers University, Department of Physics & Astronomy, 136 Frelinghuysen Rd, Piscataway, NJ 08854, USA. [7] Centro Nacional de Aceleradores, Universidad de Sevilla, CSIC and Junta de Andalucía, 41092 Sevilla, Spain. [8] Departamento de Física Atómica, Molecular y Nuclear, Universidad de Sevilla, 41012 Sevilla, Spain. [9] Molecular Foundry, Lawrence Berkeley National Laboratory, Berkeley, CA 94720, USA. [10] Department of Nuclear Engineering, University of California, Berkeley, CA 94720, USA. [11] Present address: State Key Laboratory of High Field Laser Physics and CAS Center for Excellence in Ultra-Intense Laser Science, Shanghai Institute of Optics and Fine Mechanics, Chinese Academy of Sciences, Shanghai 201800, China. [12] Present address: Fakultät für Physik, Ludwig-Maximilians-Universität München, Am Coulombwall 1, 85748 Garching, Germany. [13] Present address: Marvel Fusion GmbH, Blumenstrasse 28, D-80331 Munich, Germany. ✉email: T_Schenkel@LBL.gov

Controlling the electronic structure of semiconductors through doping and defect engineering has enabled large-scale integration of classical electronic devices[1]. Ion implantation emerged in the 1960s as an effective and economically viable method to introduce dopant atoms into semiconductor materials such as silicon[2]. Implantation of ions with energies from ~1 keV to 1 MeV is followed by thermal annealing to repair damage to the host crystal lattice that was induced during the stopping of energetic ions, to activate dopants, or to form desired defects[3,4]. A prominent example of a defect for emerging applications in quantum information science is the nitrogen-vacancy color center in diamond that can be formed by implantation of nitrogen ions followed by thermal annealing[5]. Color centers and photon emitting defects are ubiquitous in semiconductors, and have long been known to form during exposure of silicon crystals to high energy particles and photons[6]. Recently, photon emitting defect centers in silicon, including the G-center (a pair of substitutional carbon atoms bound to a silicon interstitial atom) and the W-center (three silicon interstitial atoms), have been revisited for quantum applications with single photon sources[7–10]. The promise of compatibility with CMOS processing for (ultra) large scale integration makes this particularly intriguing[10,11]. The reliable formation and placement of photon emitting centers with narrow line widths, high spectral stability and long coherence times are prerequisites for applications in quantum information science and technology with increasingly complex numbers of qubits and interconnects.

Conventional ion implanters mostly operate with continuous ion beams and current densities in the mA cm^{-2} range[3,12]. Nanosecond laser pulses and pulsed ion beams with ~100 ns pulse length and peak currents >10 A cm^{-2} from magnetically insulated diode electrostatic accelerators have been used to process materials, including early studies of simultaneous doping and annealing of silicon[4,13]. However, much shorter (sub-ns to ~10 ns) ion pulses can now be generated through the interaction of laser pulses with thin foils at intensities >10^{18} W cm^{-2}[14]. These short, intense ion pulses from laser-solid interactions are being explored for a broad range of applications[15], including inertial fusion energy[16], nuclear physics[17], (flash) radiation biology[18], studies of radiation effects in materials and materials analysis[19–21]. Most of these applications have focused on the use of high energy protons and (heavy) ions (>10 MeV). Here, we report on ion irradiation experiments of single crystal silicon samples with intense, high flux ion pulses from a laser-accelerator. Ion flux levels of 10^{22} ions cm^{-2} s^{-1} are observed in our experiments, about five orders of magnitude higher than available with conventional ion implanters that typically operate at flux levels below 10^{17} ions cm^{-2} s^{-1} (~10 mA cm^{-2}). Following exposure to a single pulse or to a series of proton and ion pulses, changes in the surface structure of single crystal silicon samples, their local chemical composition and structural and optical properties are characterized. We observe high flux doping of silicon with carbon ions and direct local formation of photon emitters in the telecom band. Laser-ion accelerators expand the parameter range for defect engineering into a high flux regime of simultaneous heating, doping and color center formation. This enables new directions in the search for and optimization of silicon based color centers with properties tailored for selected applications, such as emission of (indistinguishable) photons in a telecom band and efficient coupling to a quantum memory for applications in quantum repeaters and quantum networking[11].

Results

Laser-ion acceleration setup. Ion pulses were generated using the BELLA petawatt laser, a Ti:Sapphire laser (815 nm)[22]. Laser pulses with pulse energy of 39 J and pulse lengths of 39 fs (full width half maximum, FWHM) were focused into a ~52 μm focal spot for intensities of ~$7×10^{18}$ W cm^{-2}[23]. Laser pulses were focused onto 13 μm thick Kapton tape targets that had been spooled onto a tape drive so that thousands of shots per tape could be conducted[23] (Fig. 1). Each laser pulse forms a hole with a diameter of about 3 mm in the Kapton tape. The tape drive is advanced by ~15 mm after each laser shot. Laser ion acceleration experiments were conducted at a repetition rate of up to 0.2 Hz.

Ion spectra were measured in situ with a Thomson parabola (TP) type mass spectrometer, complemented by stacks of radiochromic films (RCF)[23,24]. Silicon samples were analyzed ex situ using secondary ion mass spectrometry (SIMS), nuclear reaction analysis (NRA) and channeling Rutherford Backscattering (ch-RBS) to quantify the fluence and depth distribution of ions implanted into the silicon samples as well as the resulting structural changes to the crystal lattice. Ion pulses were dominated by protons and carbon ions from contamination layers on the back surface of the Kapton tapes and from the disintegration of the Kapton foil. High energy proton and carbon ion energy spectra follow the well-known Boltzmann-type distribution from the Target Normal Sheath Acceleration (TNSA) mechanism[23,25]. Proton and carbon ion energies up to 8 MeV were observed in our experiments[23]. The silicon samples, positioned 25 mm downstream from the laser target foil, were irradiated using ion pulses with intensities of ~10^{12} ions cm^{-2} with energies >2 MeV[23] (Fig. 1 a). By analyzing the RCF, it was found that proton pulses had an energy-dependent divergence angle (FWHM) ranging from 8 degrees (7 MeV) to 22 degrees (2 MeV)[18], resulting in an (energy dependent) proton beam spot with a nominal diameter of ~4 to 20 mm at the position of the ion targets 25 mm downstream from the laser targets.

Fig. 1 b) shows a typical TP mass spectrum with the charge state sequence of ions dominated by C^{4+} on the phosphor screen of the multi-channel plate detector. Silicon samples were cut to approximately 1 cm^2 chips from n-type float-zone wafers with (111) orientation and a resistance of ~100 Ohm cm. The samples were partially covered with 25 μm thick aluminum foil with a 5 mm diameter aperture. The aluminum is thick enough to stop carbon ions up to an energy of about 25 MeV. This allowed for the comparison of areas on samples that were exposed to all ions (no aluminum cover) to areas that were only exposed to protons (with aluminum cover). The opening was aligned with the position of the expected peak proton and ion flux. Sample assemblies were mounted together with RCF pieces onto a target wheel that held up to eight samples.

First, the laser and laser-ion pulses were tuned using the TP and then silicon samples were exposed to a single pulse, or a series of two, ten, or one hundred pulses of laser-accelerated protons and ions. During repeated ion pulses, evaporation of the aluminum foil was observed around the opening on the silicon samples due to heating by the proton and ion pulses (see Supplementary Note 1). Ion pulses in the TNSA regime have an initial pulse length of picosecond duration. However, since the energy distribution of protons and ions is very broad, the TNSA ion pulse de-bunches along the flight path of 25 mm in our setup to about 10 ns (the flight time spread between 8 MeV protons and 0.3 MeV carbon ions).

Surface topography changes and exfoliation. Changes in the surface structure of silicon samples were characterized by optical microscopy and with a helium ion microscope. Microscope images visualize the spatial distribution of energy deposition from laser-ion pulses and the corresponding response of silicon crystals samples. Fig. 2 shows optical and helium ion microscope (HIM)
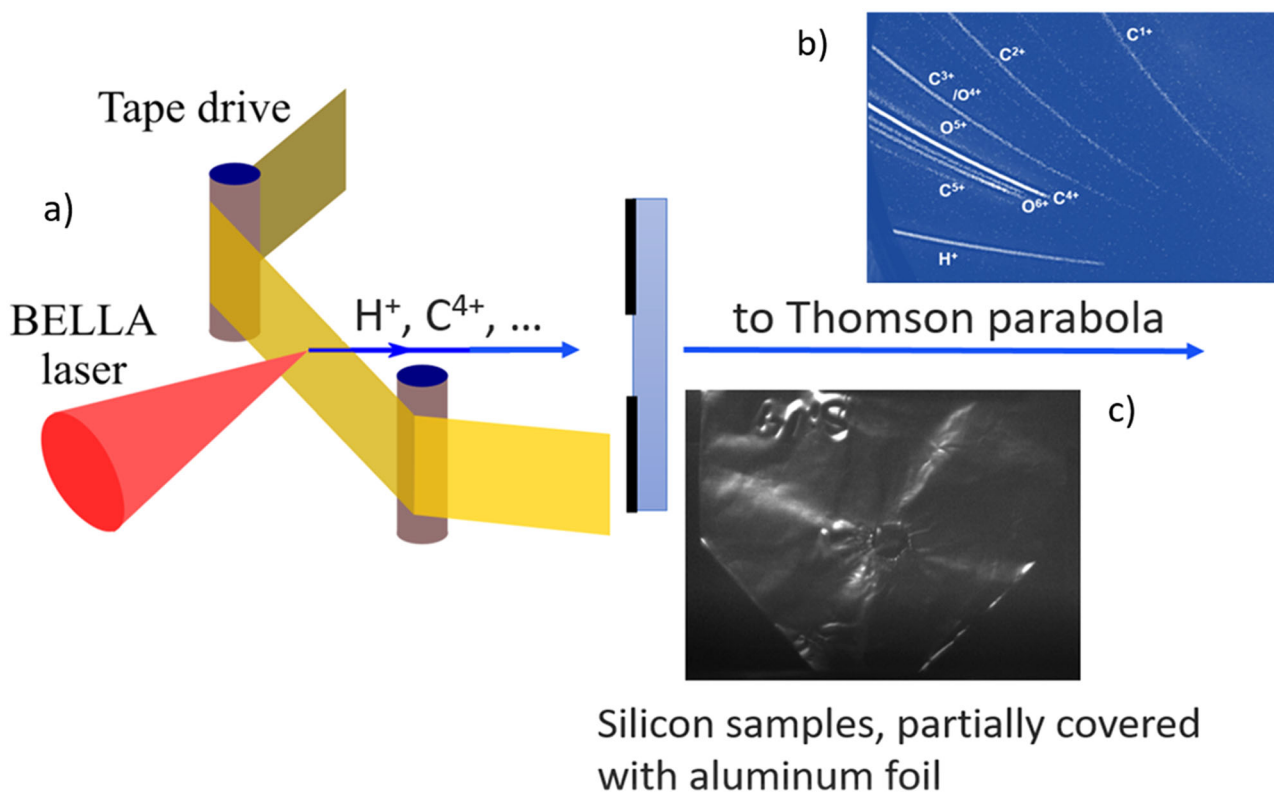
Fig. 1 Schematic of the experimental setup (not to scale). a Schematic of the tape drive and ion target assembly, **b** example of a Thomson parabola (TP) spectrum dominated by C^{4+} and protons (H^+) with energies up to 8 MeV. **c** Following tuning of laser conditions using the TP, silicon samples were inserted for exposure to proton and ion pulses. A time-lapse video of a multi-shot series is shown in Supplementary Note 1.
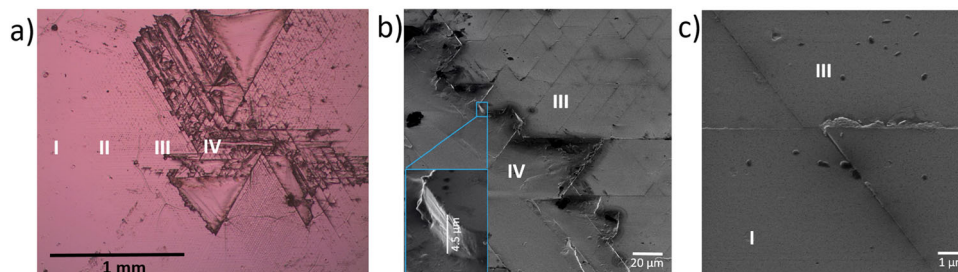

Fig. 2 Microscope images of silicon samples after exposure to a laser-ion pulse. Optical, (**a**), and helium ion microscope (HIM) images, (**b**) and (**c**), of a silicon (111) sample that had been exposed to one laser ion pulse. a) The optical image shows areas with no surface damage (I) adjacent to areas with tessellation patterns (II), (III) and exfoliation (IV). The insert in b) shows the thickness of an exfoliated layer of 4.5 µm. **c** Shows an area where a silicon tile started to peel off in response to the local ion flux (III). At the top of the exfoliating tile, re-solidified silicon that melted appears to have emerged from under the tile. Note that the HIM images show the key features of the regions labeled (III), (IV) but are not of the exact same regions marked in the optical image. Region (I) in **a**) and (**c**) is representative of the unexposed silicon, which showed no features in HIM or optical microscopy.

images (the latter obtained under an angle of 45 degrees) of a silicon (111) sample that had been exposed to one ion pulse. The optical image was taken at a magnification of 6.25x in order to provide an overview of the highly non-uniform surface topography across an area of about 6 mm^2. In the center of the image (IV), we observe a region where layers of silicon were exfoliated. These exfoliated sections are separated by a sharp transition from neighboring areas showing triangular tessellation patterns of cracks that reflect the silicon (111) crystal structure (III).

Farther away from the exfoliated areas, the cracks wane in intensity (II) and the surface transitions to areas with no obvious change in the surface structure (I). The field of view in this optical image is 2.45 mm and the characteristic features in this single pulse beam spot are shown, which covers part of the 5 mm diameter opening in the aluminum mask. Clearly, the irradiation

conditions on the sample were not uniform. The thickness of the exfoliated layers ranged from 4–7 µm, as determined from the step heights between regions (III) and (IV) measured in the HIM images; see for example, the HIM image in Fig. 2 b). The HIM image in Fig. 2 c) shows cracks in the silicon and the onset of an incomplete exfoliation event, with what appears to be re-solidified silicon that melted and flowed out from under the exfoliating tile. The total area in which exfoliation is observed covers about 1 mm^2, much smaller than the 20 mm^2 nominal ion beam spot. The corresponding ion pulse full divergence angle to cover a ~1 mm^2 spot with peak intensity is only 4.6 degrees, smaller than the earlier result for 8 MeV protons from RCF analysis[18,23].

The findings reported here show that optical monitoring of damage on a silicon chip can provide rapid in situ feedback on proton and ion pulse properties and support tuning of desired
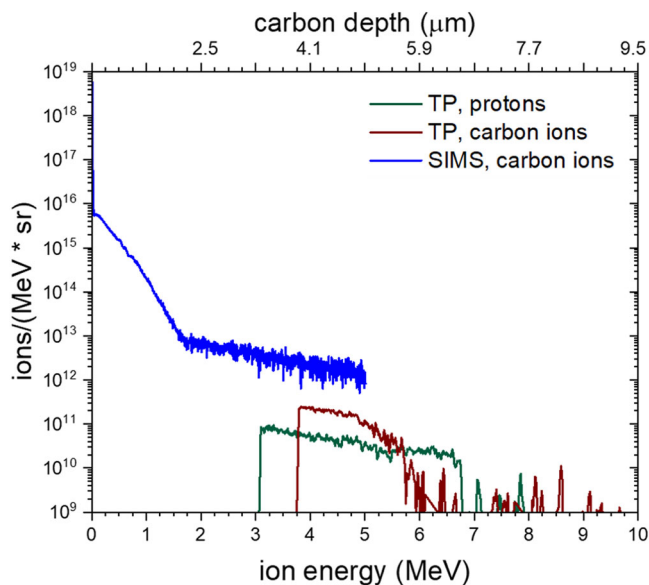
Fig. 3 Examples of Thomson parabola (TP) data for protons and C^{4+} ions, together with a Secondary Ion Mass Spectrometry (SIMS) depth profile for all carbon ions. The red lines show extrapolations of the TP and SIMS data to low energies. A carbon concentration from SIMS of 10^{16} atoms cm^{-3} corresponds to 10^{13} ions $MeV^{-1}sr^{-1}$ in the comparison with TP data.

Fig. 4 Simulations of the silicon sample temperature as a function of depth for a series of time steps following a laser-ion pulse. Details of the energy deposition to temperature profile calculations are provided in the Supplementary Note 3. The dash-dot line shows the melting temperature of silicon of 1683 K; the dotted line shows the boiling temperature of silicon of 2628 K.

laser ion acceleration conditions, complementing TP measurements (which can be affected by the narrow acceptance angle in a TP mass spectrometer). The surface damage results from all ions, and thus also complements the RCF stacks, which are only sensitive to MeV protons. The highly non-uniform damage patterns point to possible structures in the proton and ion pulse (e. g. from microscopic non-uniformities in the Kapton foil), filamentation effects due the Kapton being insulating, and to possible structure in the laser pulse[26,27].

Ion pulses and local heating of silicon. Having observed highly non-uniform surface topography changes, we now analyze the local energy deposition from single and repeated ion pulses and estimate the resulting surface temperature profiles in silicon. SIMS was used to characterize the local carbon, oxygen and hydrogen implantation fluences in order to complement the TP data on proton and carbon ion intensities (Fig. 3). We also note that SIMS can cross calibrate TP spectra. TP based mass spectrometry can capture single shot events with broad ion species and energy distributions, and to resolve ion species, a small pinhole aperture is required. For this purpose, an opening with a diameter of 0.3 mm about 1 m downstream from the laser target was used, which limited the field of view of the mass spectrometer. The microscope images above show irradiation with a highly non-uniform ion pulse across the samples and reveal jet-like locally enhanced ion intensities, which can be missed or only partially captured with a TP.

The SIMS sensitivity for carbon in silicon was about 10^{16} atoms cm^{-3}[28]. To compare the SIMS results with the TP results, samples were analyzed that had been exposed to a series of ten ion pulses to accumulate a carbon concentration well above the sensitivity limit of SIMS in the top ~5 μm of the sample. Depth profiles were dominated by carbon, with lower concentrations of oxygen and hydrogen that followed the trend in the local variations of carbon concentrations (see Supplementary Note 2). In Fig. 3, SIMS and TP data are compared after normalizing the SIMS data to concentrations per ion pulse. The depth-energy relation of carbon ions in silicon was estimated using the
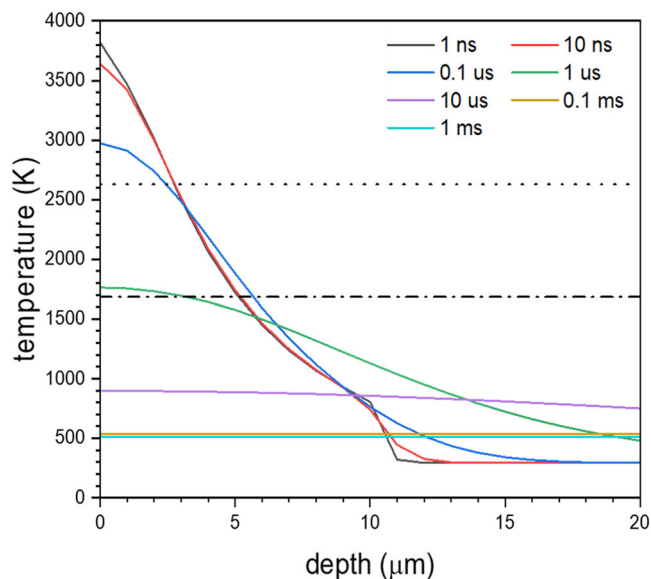
"Stopping and Range of Ions in Matter (SRIM)" code[29]. The slope of the carbon depth profile from SIMS was found to be approximately the same as the slope of the proton and carbon ion intensities as a function of energy above the low energy cutoff of about 3.5 MeV from our TP settings. The SIMS data include all carbon species, while the TP data in this example are for the dominant C^{4+} species only.

When calculating the extrapolations shown in Fig. 3, it was assumed that the dominant contribution to the proton and ion flux is from TNSA and the exponential ion energy distribution from TNSA was extrapolated to zero ion energy. The resulting local, peak energy deposition from energetic protons and ions is about 2 J cm^{-2}. Other mechanisms, however, can also contribute to the low energy ion flux, including plasma expansion[30] and disintegration of the Kapton foil. In samples that had been exposed to single ion pulses we observe carbon concentrations up to 10^{20} atoms cm^{-3} with a peak depth of 200 to 500 nm. If these carbon atoms were implanted with average ion energies of 50 to 200 keV (corresponding to implantation depths of 150 to 500 nm) then the energy deposition for a fluence of ~10^{15} ions cm^{-2} would locally reach ~30 J cm^{-2}. Analytical calculations and finite element analysis of the corresponding temperature rise show heating to temperatures well above 10^4 K for intensities of 30 J cm^{-2}, which seems unrealistically high given the observed surface structures.

This high fluence of near-surface carbon stems from the deposition and implantation of very low-energy carbon ions associated with the plasma expansion of the Kapton foil following the intense laser pulse. In Fig. 4, calculated temperature profiles are shown as a function of time based on the ion energy deposition extracted from the SIMS and TP spectra and using known values for the thermal conductivity of silicon. The high peak temperature of 3750 K can be considered a lower limit based on the extrapolation of the ion spectra. We find that the peak temperature drops below the melting point of silicon of 1683 K after about 1 μs following the ~10 ns long ion pulse. Given the thermal conductivity and heat capacitance of silicon, the peak temperature reached at a depth of 6 μm roughly equals the
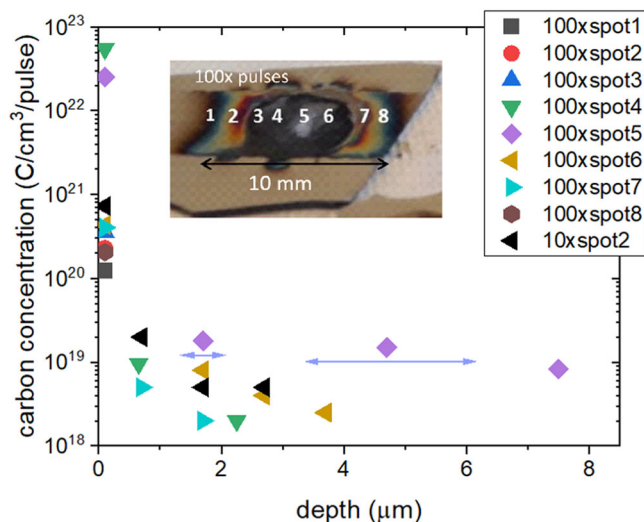
Fig. 5 Nuclear reaction analysis (NRA) of carbon concentrations. Depth profiles of carbon for NRA spots on the 100x pulse sample and for the central beam area on the 10x pulse sample ("spot 2", Supplementary Note 4). The depth intervals of 1 to 3 µm used for signal integration are indicated by the arrows. Peak carbon concentrations in spot 4 equal the density of silicon atoms of 5×10^{22} atoms cm^{-3}.
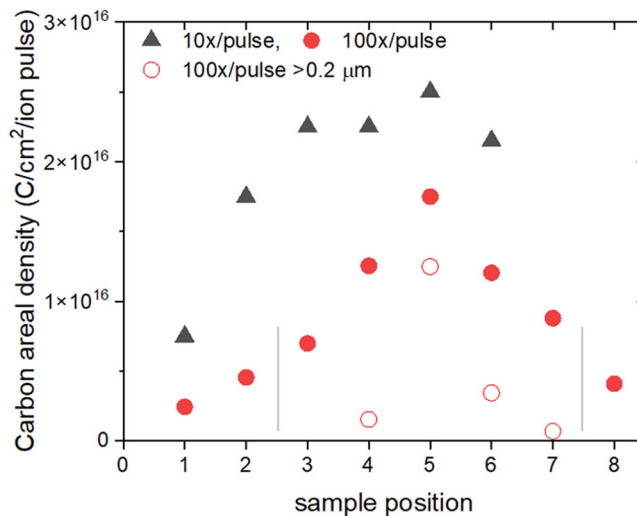

Fig. 6 Carbon areal density near the surface. Line scan of carbon areal density in the top 200 nm for the 10x and 100x pulse samples for the series of NRA spots across the laser-ion beam spot in a 10 mm line scan. For the 100x pulse sample we also show the carbon areal density integrated for depth >200 nm. The concentration and areal density values are normalized to the number of pulses for comparison. The gray lines indicate the initial 5 mm wide opening in the aluminum foil.

melting temperature of silicon. This depth coincides with the thickness of the exfoliated layers observed in microscope images (Fig. 2). Details on the temperature profile calculations are provided in Supplementary Note 3.

Exfoliation is observed on samples that had been exposed to one single ion pulse, as well as for a series of ion pulses. The thickness of exfoliated layers is similar to that reported earlier for a series of over ten 100 ns long ion pulses from an electrostatic ion accelerator and energy deposition of about 1 J cm^{-2}[31] where the peak silicon temperature had been evaluated to be 1600 K, about two times lower than for our conditions.

Nuclear reaction analysis of carbon in silicon. The superposition of MeV protons and carbon ions from TNSA and a pulse of much lower energy ions from plasma expansion poses a challenge in understanding the local energy deposition and temperature evolution. To elucidate the relative contributions of TNSA ions and ions from plasma expansion, samples that had been exposed to 10x and 100x ion pulses were analyzed using the Nuclear Reaction Analysis (NRA) technique[32]. Details on NRA are presented in the Supplementary Note 4.

Fig. 5 shows the carbon concentrations of samples from 10x and 100x ion pulses as a function of depth for a series of analysis spots across the samples. NRA is based on inducing nuclear reactions between MeV projectile ions and host atoms in the sample. NRA is therefore insensitive to chemical effects, or so called matrix effects, that can affect SIMS depth profiles in the presence of very high impurity concentrations and in the presence of surface roughness, which are both present in our samples. But the sensitivity, lateral (~0.1 mm) and depth resolutions (a few nm) of SIMS far exceed those of NRA. NRA shows peak carbon concentrations equal to the density of silicon atoms, i. e. 5×10^{22} cm^{-3}, in the top 200 nm. We observe carbon at a depth greater than 200 nm only for the central area of the sample ("spot 5" for the 100x sample). In this central area, carbon is found at a depth as deep as 7.5 ± 1.5 µm at a concentration of 8.3×10^{18} C-atoms cm^{-3} (where we have normalized the concentrations to the number of ion pulses).

Fig. 6 shows a line scan of NRA profiles across the 10x and 100x pulse samples indicating a profile of carbon areal densities peaking at $1.7–2.5 \times 10^{16}$ C-atoms cm^{-2} per pulse. When we plot the areal density of carbon at a depth larger than 200 nm for the 100x pulse sample we see that it is localized near the center of the sample (spot 5). A fraction of these carbon atoms stem from high energy ions that were implanted. Most of the carbon is very close to the surface. In the center of the samples, where we also observe the most intense damage, we see carbon to a depth of over 7 microns. We belief that most of the carbon comes from plasma expansion and the disintegration of the Kapton foil. MeV ions from TNSA reach the silicon sample after a flight time of few ns and can locally heat and melt the silicon. Low-energy carbon ions with energies as low as ~100 eV reach the silicon sample after a flight time of ~1 µs, around the time when the temperature drops below the melting point in our estimate. Once low-energy carbon ions impinge on the hot and molten silicon surface, they can rapidly diffuse and redistribute in the top few microns of the sample, until the silicon cools and (partially) recrystallizes after >1 µs.

NRA scans (with analysis spots of 1 mm diameter, along a 10 mm long line scan across the sample) were complemented with the SIMS depth profiles (with analysis spots of 0.1 mm diameter, line scan over ~1 mm on the sample) shown in Fig. 7. The SIMS spectra of a sample that had received one ion pulse (see Fig. 2) show a progressively increasing depth of carbon atoms with a slowly varying integrated areal density (see insert in Fig. 7). A control sample that had not been exposed to ion pulses showed a near-surface profile of carbon with an areal density of 3.5×10^{14} C-atoms cm^{-2}, which is much lower than the observed carbon areal densities across exposed samples. The deepest carbon profiles are observed closest to the highly damaged area.

Inside the exfoliated area, SIMS depth profiles became unreliable due to the highly textured surface. This trend in the SIMS profiles is consistent with the NRA result and supports the interpretation of local carbon drive-in and diffusion, with a smaller contribution of high-energy carbon ions. Following 1x, 10x and 100x ion pulses, carbon atoms accumulate near the surface of samples and are also driven progressively deeper into the silicon.

Low-energy carbon atoms are driven into the silicon sample due to the high local energy deposition and heating from the high energy ion pulse(s). This is analogous to laser-driven atom in-diffusion into silicon with laser pulses of similar duration (few ns) and intensity (few J/cm^2)[33]. In gas immersion laser doping, adsorbate layers on the surface are used as the source of the atoms that are diffused into the material[34]. Thus, a major difference is that the doping atoms, carbon in our present experiments, originate from the plasma expansion of the laser foil target (here Kapton). A choice of a different material for the laser foil target will enable high flux, high-fluence doping with other selected species (e.g., boron, gold or titanium). Hence, a new high-flux

surface doping process, referred to as "laser-ion doping", was observed that is complementary to gas immersion laser doping[34]. In laser-ion doping, peak surface dopant concentrations well in excess of 1 atomic % are observed from single ion pulses. In comparison, tens of laser pulses are required in gas immersion laser doping to achieve similarly high concentrations. Characterization of the electrical properties of materials with very high dopant concentrations from laser-ion doping is the subject of ongoing studies.

Microscopies of surface topography changes and the compositional analysis of the samples by SIMS and NRA are further complemented with channeling Rutherford Backscattering (ch-RBS) measurements (see Supplementary Note 5). Ch-RBS is used to track the structural evolution of silicon crystal samples for a series of 1, 2, 10 and 100 ion pulses. Ch-RBS is sensitive to the areal density of displaced atoms[35]. Ch-RBS showed that the density of displaced silicon atoms increased with the increasing number of ion pulses. However, point defect concentrations stayed well below levels that would indicate the presence of amorphous silicon layers from the accumulation of radiation damage. This is consistent with damage annealing in the high thermal budget from ion energy deposition. It is also consistent with the formation of dislocation loops in the highly carbon-doped silicon samples.
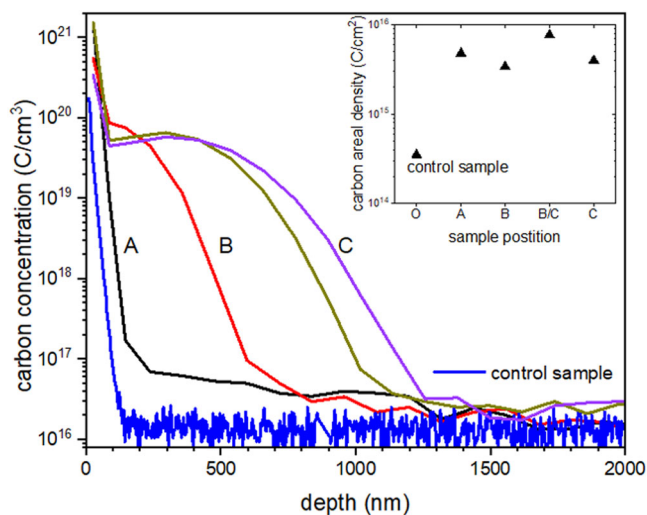
Color center spectra. Having characterized surface structure changes, the flux of implanted carbon ions and the resulting temperature changes, resulting changes in the optical properties of silicon samples are now discussed.

Following exposure to a single pulse or to a series of ion pulses, low-temperature photoluminescence (PL) measurements were conducted to characterize the resulting color center spectra. Fig. 8 shows a 5 mm wide line scan of PL spectra. The measurement temperature was 3 K. The silicon sample had been exposed to two laser-ion pulses. Continuous wave excitation at 532 nm was used for the PL measurements. Comparing the results from several samples that had been exposed to the same number of ion pulses results were found to be reproducible. The detailed local irradiation conditions, surface changes and resulting color center
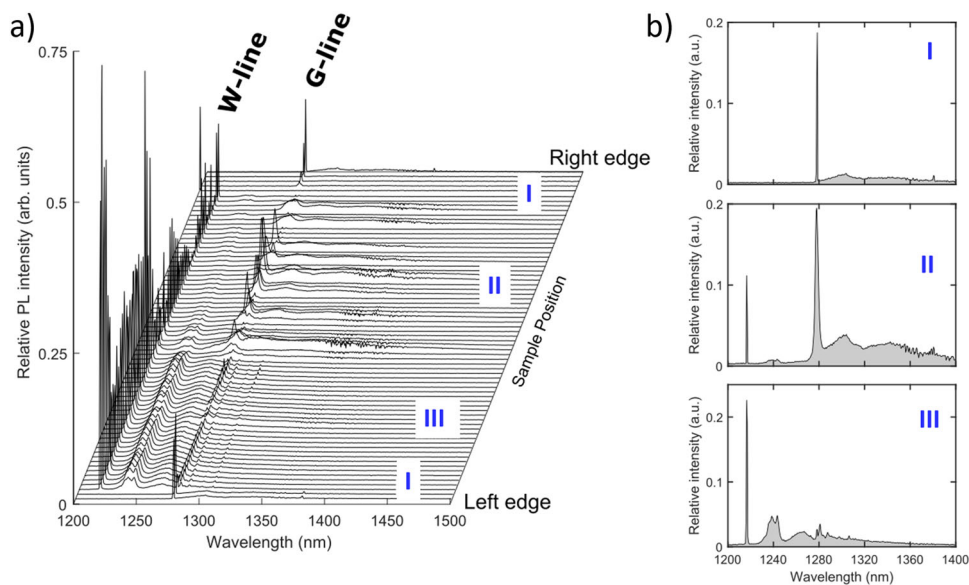

Fig. 7 Secondary ion mass spectrometry (SIMS) depth profiles of carbon in a silicon. SIMS depth profiles. from a sample that had been exposed to one laser-ion pulse for a series of positions across 1 mm of a sample with positions A, B, C corresponding to I, II, III in Fig. 2. The insert shows the carbon areal densities for the series of positions. A carbon concentration of 10^{20} C-atoms cm^{-3} corresponds to 2000 ppm.

Fig. 8 Photoluminescence (PL) spectra across a sample after exposure to laser-ion pulses. a Line scan of low temperature (3 K) Photoluminescence (PL) spectra taken across a silicon (111) sample that had been exposed to two laser-ion pulses. **b** Spectra from the left and right edge of the sample where we observe only G-centers, corresponding to the area labeled (I) in the optical microscope image shown in Fig. 2. Areas with increased ion flux show both W and G-centers, corresponding to area (II) in Fig. 2. Regions with higher local ion flux show mostly W-centers, (III) in Fig. 2.

distributions varied, however. PL spectra were dominated by emission lines centered at 1217 nm and 1278 nm, corresponding to the well-known W and G-centers in silicon, respectively[6–8].

We see an intense signal from G-centers at 1278 nm from a region on the sample that had been masked by the 25 μm thick aluminum foil during the irradiation. The aluminum foil stopped all carbon ions and also protons with energies up to about 1.4 MeV. The spectrum of higher energy protons is downshifted by energy loss in the foil. This also results in a shortening of the proton pulse to sub-ns duration, because the low energy tail of protons is stopped in the aluminum foil. Energetic protons form silicon interstitials in close impact parameter collisions and these can then diffuse towards the surface where they can combine with substitutional carbon pairs, forming G-centers[36]. The exact spectrum of these protons is not known because the TP has a low energy cutoff of about 3 MeV in our measurements. The concentration of carbon near the surface was determined by SIMS analysis of control samples and samples that had been covered with aluminum foil (see Fig. 7, and in the Supplementary Note 2). Carbon depth profiles from masked areas resemble those of control sample. These SIMS data constrain a possible contribution of carbon that can diffuse into masked areas from the unmasked beam spot.

Formation of G-centers from irradiation of silicon that contains carbon is well known[6]. Direct local formation of G-centers with carbon that was already in the lattice and with silicon interstitials formed by energetic protons represents an elegant way to locally add G-centers into silicon. This technique could also be used to add G-centers into fully integrated silicon devices without any subsequent thermal annealing. The high flux of protons, estimated to be 10^{11} protons cm^{-2} ns^{-1} from the TP data and given the divergence angle of the proton pulse, can aid G-center formation if the mobility of silicon interstitials is increased due the transient local excitation and heating of the matrix[37]. The ability to tune the proton flux from a compact laser accelerator now extends the parameter space for local G-center formation.

In areas that had been exposed to both proton and carbon ions spectra with G as well as W-centers are observed (spectrum (II), Fig. 8 b). Comparing results from several single and two pulse samples we found that W and G-centers are formed in areas of intermediate ion flux and local heating, areas (areas (II) in Fig. 2). In regions with higher local energy deposition, only W-centers are observed (area (III)). The line width of the G-centers increases significantly in areas of higher surface damage and higher carbon concentrations from higher ion flux conditions, while the width of the W-center peak does not increase. The transition from areas with both G and W-centers to those with only W-centers also maps to the relative temperature stability of these centers. G-centers are significantly more likely to dissolve at temperatures as low as 470 K, while W-centers have been reported to be stable up to at least 600 K[6–8]. These temperatures appear very low considering the much higher peak temperatures we estimate from our ion pulse conditions. This points to the important difference in thermal budgets applied over an extended period (>1 s) in conventional thermal annealing in contrast to the condition of very rapid heating (~3700 K in 10 ns, or >10^{11} K s^{-1}) and cooling (~3x10^9 K s^{-1}). During rapid heating and cooling, specific defect configurations can be formed and stabilized before they dissolve. PL spectra are shown in the Supplementary Note 2 together with SIMS depth profiles that had been taken prior to PL at the same locations on the sample.

Density Functional theory (DFT) of G and W-centers vs. local disorder. Having observed local color center formation for a series of irradiation conditions DFT calculations were conducted to understand the sensitivity of W and G-centers to local

disorder. To model the electronic properties of these defects G-center Type-B[29,38–41] and W-center Type-V[41–44] structures were used. To determine the sensitivity of the defect energy levels to perturbations in the local environment, these structures were first relaxed, and then used as a starting point for quantum molecular dynamics (QMD) simulations. We let the structures evolve for 3 to 5 ps after thermalization and then collected the defect energy levels at each time step. These energies are computed using the PBE functional (see Methods), which is known to underestimate the magnitude of the insulating gap. Nevertheless, the fluctuations around the average value are expected to reproduce the correct trends for these defect centers.

QMD simulations were used to understand the sensitivity of G-center and W-center defects to local disorder. While the structural fluctuations arise from thermal effects in our simulations, they can also be used to probe the dependence of optical properties on inhomogeneous broadening effects that arise due to static disorder. This is because local disorder, induced by other distant defects in the dilute limit, can be understood as low-energy distortions which are well-represented by thermal fluctuations of the QMD trajectories.

The results from QMD simulations are presented in Fig. 9 and show two apparent trends. Firstly, at each temperature the distributions for the G-center are broader than for the W-center. This is consistent with the observed narrower linewidth of the W-center emission spectra reported above. Secondly, Fig. 9 shows that the effect of increasing temperature, and hence, increasing disorder, is more pronounced for the G-center than the W-center. At lower temperatures the slope of the spread is steeper for the G-center than for the W-center. It should be noted that this estimate of linewidth broadening is limited by the finite size of the simulation cell. Periodic boundary conditions place defect centers in close proximity to their images in adjacent unit cells, leading to possible interactions, while the finite size sets a limit on the allowed phonon-frequencies. These effects lead to a systematic overestimation of the broadening for both types of defect centers, but the trends and relative magnitudes can still be compared. The main conclusion that can be drawn is that in order to obtain G-centers with narrow linewidths, low disorder will be essential, which informs strategies for process optimization. On the other
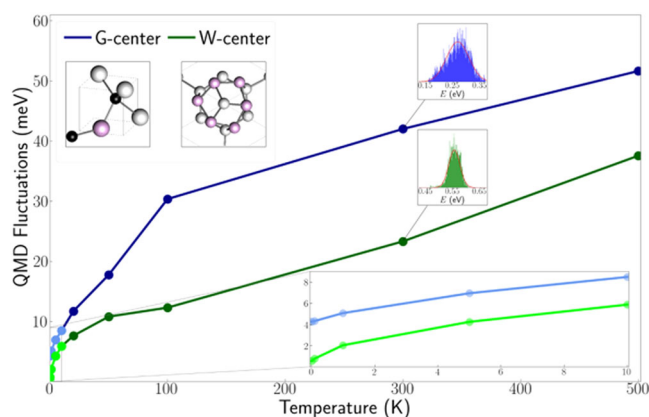

Fig. 9 Quantum Molecular Dynamics (QMD) simulations for W and G-centers vs. simulation temperature, which represents local disorder. The G-center shows a higher sensitivity to disorder than the W-center, in agreement with experimental results. Insets (top left) show G and W-center structures with C-atoms in black, Si-atoms in gray, and defect (interstitial) Si-atoms in pink. Each point in the plot represents ~5000 configurations obtained through QMD. Inset (bottom right) shows a magnified region of the plot for 0–10 K. Sample histograms (top right) of this data are shown at 300 K for both defect centers.

hand, the W-center is more robust to disorder, which is a promising property given that the creation of a W-center requires the formation of three silicon interstitials and is often associated with high damage events and processes.

The effect of excess interstitial carbon on the electronic structure of the defects was also analyzed. Neutral carbon defects were inserted at each of the 106 possible tetrahedral interstitial sites[36] within the $3 \times 3 \times 3$ silicon supercells hosting the W and G-center defects. Excess carbon interstitials have a similar effect on the two defect structures. The Supplementary Note 6 include scatter plots showing the defect gaps and energies for varying distance between carbon interstitial and defect center. Here the trend is more subtle. While, unsurprisingly, both centers have significant variation in their defect properties when carbon interstitials are in close proximity, in the real samples, the carbon concentration of order 1 atomic % are reached only when in very close proximity to the sample surface (i. e. the top ~200 nm, while the PL probes a depth of ~1 μm). When considering the configurations where the carbon interstitial is farther away (10–12 Å), the properties of the G-center experience much greater variation than those of the W-center. The relative stability of the G-center and W-center to perturbations can be understood from a structural standpoint. Currently, the structure of the G-center is believed to be the B-type configuration, which can be seen as two substitutional carbons and a twofold coordinated interstitial silicon between them, forming a C_s-Si_i-C_s dumbbell structure. When this structure was first proposed, it was already noted that this dumbbell structure has three possible orientations around the substitutional carbons, explaining the C_{3v} rotational symmetry observed in electron paramagnetic resonance (EPR) spectra[38]. It has also been suggested that this center could transform to a related A-type structure 0.02 eV higher in energy through a bond switching process that would generate threefold coordinated Si_s and C_s[38]. More recently, it has been shown that the low coordination of the B-type structure allows it to rotate about the [111] axis through several local minima[9,38]. Conversely, each silicon atom comprising the W-center structure is covalently bonded to four nearest neighbors in a tetrahedral arrangement, which is much less susceptible to structural distortions.

Discussion

Analyses of silicon samples exposed to single pulses or a series of pulses of laser-accelerated ions show two distinct contributions to the total ion fluence. The first contribution is from MeV ions that form an intense, short (1 to 10 ns) pulse from laser acceleration through TNSA with a typical fluence of ~10^{12} cm^{-2} and local energy deposition up to ~2 J cm^{-2} in our experimental setup. A second pulse of very low-energy ions and particles, with kinetic energies <10 keV, is formed through plasma expansion and the disintegration of the laser-foil target (here Kapton). We find that the fluence of these low-energy ions and particles is ~10^{16} cm^{-2}, about four orders of magnitude higher than that for protons and ions from TNSA. The low-energy ions trail the MeV ions, and can arrive at the silicon samples when it is still hot or locally molten. Low-energy ions with a kinetic energy of ~100 eV can reach the silicon surface within 1 μs in our setup, fast enough to then quickly diffuse into silicon that is still heated to a temperature close to the melting point.

This high flux surface doping process is analogous to gas immersion laser doping[33,34], but now with spatio-temporal alignment of a high energy ion pulse followed by a pulse of low energy dopant ions and particles in a laser accelerator. This finding opens a new direction for exploration of high flux surface doping and synthesis of materials[34,45]. Carbon concentrations of more than several atomic % per ion pulse are observed near the surface of silicon. This suggests that very highly doped materials

phases might become accessible with this approach. Laser-foil targets, including boron or other dopants, can be prepared in situ to reduce the effect of common surface contaminants for synthesis of materials with tailored properties (e.g. superconductivity in covalent semiconductors with high boron concentrations)[27,34,45].

Highly non-uniform surface topography changes are observed across the 5 mm nominal ion beam spot. The regions where silicon is exfoliated are structured and do not represent simple Gaussian ion pulse shapes. High flux regions showing exfoliation cover about 1 mm^2, indicating full divergence angles in the high energy ion pulses of ~4.5 degrees. In situ optical microscopy at low magnification (~5x to 10x) can be used in future studies to characterize the local ion intensity using damage on silicon targets. This can support rapid tuning of laser parameters and optimization of the experimental setup in laser-ion acceleration experiments.

Exfoliation of silicon (100) following exposure to ~50 ion pulses from an electrostatic accelerator and from exposure to high flux low energy plasma flows have been reported earlier[31,46]. Here, we find local exfoliation from single ion pulses. In laser-ion acceleration using TNSA, the carbon and proton ions de-bunch to about 10 ns in our setup with an ion flight distance of 25 mm. This pulse length is much shorter than the pulses used in earlier studies[31] using a conventional ion acceleration mechanism. The depth of the exfoliated silicon layers is the same for both types of pulsed ion beams and plasmas, reflecting the thermal properties and response of silicon to rapid surface heating in short ion pulses. The sharp transition from exfoliated areas to areas that exhibit cracks in tessellation patterns point to a phase transition across the melting point for the onset of exfoliation. Our analysis of the ion energy deposition and resulting temperature increase shows that the sample cools below the melting point within about 1 μs. However, measurements of the energy-dependent local ion flux contributions from TNSA and plasma expansion will need to be improved to refine these estimates.

Bright near IR emission is observed from G-centers that are formed locally by proton pulses and with carbon that is already present in the silicon lattice[37]. A tunable flux of laser-accelerated protons could be directed to selected regions using e. g. a plasma lens[18,33] to add G-centers into completed silicon devices (most of which contain some carbon, especially near the surface) with a compact laser accelerator. This local addition of color centers with MeV protons also occurs naturally with protons and other high energy cosmic radiation, and can be considered as a hardware error mode for future quantum devices that include color centers in silicon, or other photon sources, together with sensitive single photon detectors[11]. Quantifying the radiation hardness of emerging quantum devices is becoming increasingly important as qubit integration advances and can also be addressed with compact laser accelerators[47,48].

Color centers form directly in response to local excitation where the balance of damage formation and annealing leads to the formation of W and G-centers with varying relative intensities. Rapid local heating and quenching on the 10 ns and 1 μs time scale, respectively, can aid the formation and stabilization of color centers that would dissolve during conventional thermal annealing steps of much longer duration. DFT calculations of color center emissions as a function of local disorder agree with the experimental observation of stronger linewidth broadening of G-centers vs. W-center ensembles in high ion flux regions. We note that understanding this broadening underpins the application of these color centers for local measurements of local damage and stress fields in silicon, as well as their potential application in high-radiation environments.

Conclusions

Defect engineering and doping of semiconductors by ion irradiation and ion implantation have enabled the large-scale

integration of classical electronic devices[1–3,12]. Emerging quantum devices with spin-photon qubits can also be formed using these ion beam techniques[5,10,11]. While widely used and powerful, currently available ion beams are also limited in ion flux. High-intensity, high-power laser pulses accelerate ions from thin foils. We have quantified the properties of these ion pulses and have characterized a dual pulse structure with low energy (<10 keV) and high energy (>1 MeV) ions. Low energy ion fluences of $\sim 10^{16}$ cm^{-2} are observed, about four orders of magnitude higher than the fluence of the high energy (MeV) ions that had been the sole focus of many earlier studies of laser-ion acceleration. This dual pulse structure leads to transient heating of samples by the faster ions that arrive at the sample first. Lower energy ions from plasma expansion of the laser-foil target are then implanted into the pre-heated sample. This condition of preheating and high-flux implantation cannot be reached with conventional ion beam techniques. In areas of highest energy deposition silicon samples become highly damaged and exfoliate. However, the local ion flux can be tuned in future experiments to balance local heating, doping and the formation of desired defects and color centers.

Our results demonstrate a new form of defect engineering, high flux doping and direct local color center formation in semiconductors. With increased control of laser parameters and local ion flux conditions, intense, pulsed ion beams from (compact) laser accelerators open up new regimes and expand the parameter range accessible for materials synthesis far from equilibrium. Laser-ion accelerators enable the exploration of novel materials phases and color centers that can be formed and stabilized under conditions of rapid local excitation, doping and quenching.

Methods

Petawatt laser system. The experiment was performed using the BELLA PW laser facility at LBNL[22]. The BELLA PW laser is the world's first 1 Hz repetition rate 1 PW Ti:Sapphire laser system based on a double-chirped pulse amplification architecture, where a cross-polarized wave (XPW) contrast enhancement system is installed in between two CPA stages, delivering ~35 J laser pulses with a duration down to ~35 fs FWHM at 815 nm central wavelength. For the experiments here, a 13.5 m focal length off-axis parabolic mirror is used to focus the laser pulses to a ~52 μm (FWHM) beam spot size, yielding a peak intensity of ~7x10^{18} W cm^{-2}[22,23]. The Strehl ratio was >0.8[22,23]. The laser was operated at a pulse length of 39 fs, optimized for maximum proton energy[23]. Although 1 Hz operation would be possible, the experiments were performed with a repetition rate of 0.2 Hz.

Tape-drive target[49]. Kapton tape ($C_{22}H_{10}N_2O_5$) with a thickness of 13 μm was irradiated under a 45-degree angle of incidence. In our target assembly, the Kapton tape is spooled into a feedback-controlled tape drive system, and moved by two DC-motors, providing a fresh wrinkle-free target surface with a position repeatability <10 μm. The tape drive is capable of operating at a repetition rate of 1 Hz.

Helium ion microscopy. A Zeiss ORION NanoFab instrument was used to image silicon samples using 25 keV helium ions with a beam current of 1.35 pA and a nominal beam spot size of 0.5 nm. Images were acquired using an Everhart-Thornley detector to collect secondary electrons for a sample tilt angle of 45 degrees.

Secondary ion mass spectrometry. SIMS analysis was conducted by colleagues at EAG (www.EAG.com).

Rutherford backscattering analysis. We conducted RBS measurements with channeling analysis using 2 MeV helium ions and 1 mm beam spots.

Nuclear reaction analysis. We conducted NRA measurements on silicon samples with 1.4 MeV deuterium ion beams and using the (d, p) reactions, also with 1 mm beam spots.

Heat analysis. We conducted the analysis of sample heating for a series of ion pulse conditions using the SRIM code (www.srim.org) to extract energy deposition profiles and applying finite element analysis methods.

Photoluminescence. The PL spectra were recorded at 3 K using a scanning confocal microscope optimized for near-infrared spectroscopy. Optical excitation was performed with a 532 nm continuous wave laser focused onto the sample through a high-numerical-aperture microscope objective (NA = 0.85). The excitation power, measured at the entrance of the objective lens, was fixed at 1 mW. The PL signal was collected by the same objective and directed to a spectrometer coupled to an InGaAs Camera (900–1620 nm at -80C). The absorption depth of photons at the excitation wavelength of 532 nm is about 1 μm in silicon and this sets the depth across which color centers are probed.

Density functional theory. Numerical simulations of silicon defects were performed using the Vienna ab initio Simulation Package (VASP)[50–53]. Initial defect structures were relaxed using the HSE06 functional[41,54] using an energy cutoff of 400 eV and converged within an energy tolerance of 10^{-8} eV and forces of 0.01 eV Å^{-1} at the Gamma point. Quantum molecular dynamics (QMD) simulations used a finite temperature canonical ensemble with an Andersen thermostat[55]. Modified defect structures are relaxed using PBE functionals[56] and the same tolerance parameters used for the original structures.

Data availability

Data will be made available for reasonable requests.

References

1. Chang, C. Y. & Sze, S. M. *ULSI Technology*. (McGraw-Hill Science, Engineering & Mathematics, 1996).
2. Eriksson, L., Davies, J. A. & Mayer, J. W. Ion implantation studies in silicon. *Science* **163**, 627 (1969).
3. Nastasi, M. & Mayer, J. W. *Ion Implantation and Synthesis of Materials*. (Springer Science & Business Media, 2007).
4. Skorupa, W., and Schmidt, H. (eds.) *Sub-second annealing of advanced materials: Annealing by lasers, flash lamps and swift heavy ions*. (Springer International Publishing, 2013).
5. Doherty, M. W. et al. The nitrogen-vacancy colour centre in diamond. *Phys. Rep.* **528**, 1 (2013).
6. Davies, G. The optical properties of luminescence centres in silicon. *Phys. Rep.* **176**, 83 (1989).
7. Redjem, W. et al. Single artificial atoms in silicon emitting at telecom wavelengths. *Nat. Electr.* **3**, 738 (2020).
8. Durand, A. et al. Broad Diversity of Near-Infrared Single-Photon Emitters in Silicon. *Phys. Rev. Lett.* **126**, 083602 (2021).
9. Udvarhelyi, P., Somogyi, B., Thiering, G. & Gali, A. Identification of a Telecom Wavelength Single Photon Emitter in Silicon. *Phys. Rev. Lett.* **127**, 196402 (2021).
10. Bergeron, L. et al. Silicon-Integrated Telecommunications Photon-Spin Interface. *PRX Quantum* **1**, 020301 (2020).
11. Moody, G. et al. Roadmap on integrated quantum photonics. *J. Phys. Photonics* **4**, 012501 (2022). 2022.
12. Poate, J. M. & Saadatmand, K. Ion beam technologies in the semiconductor world (plenary). *Rev. Sci. Instrum.* **73**, 868 (2002).
13. Hodgson, R. T., Baglin, J. E. E., Pal, R., Neri, J. M. & Hammer, D. A. Ion beam annealing of semiconductors. *Appl. Phys. Lett.* **37**, 187 (1980).
14. Macchi, A., Borghesi, M. & Passoni, M. Ion acceleration by superintense laser-plasma interaction. *Rev. Mod. Phys.* **85**, 751 (2013).
15. Schreiber, J., Bolton, P. R. & Parodi, K. Invited Review Article: 'Hands-on' laser-driven ion acceleration: A primer for laser-driven source development and potential applications. *Rev. Sci. Instrum.* **87**, 071101 (2016).
16. Bartal, T. et al. Focusing of short-pulse high-intensity laser-accelerated proton beams. *Nat. Phys.* **8**, 139 (2012).
17. Boller, P. et al. First on-line detection of radioactive fission isotopes produced by laser-accelerated protons. *Sci. Rep.* **10**, 17183 (2020).
18. Bin, J. et al. A new platform for ultra-high dose rate radiobiological research using the BELLA PW laser proton beamline. *Sci. Rep.* **12**, 1 (2022).
19. Barberio, M. et al. Laser-accelerated particle beams for stress testing of materials. *Nat. Commun.* **9**, 372 (2018).
20. Barberio, M., Veltri, S., Sciscio, M. & Antici, P. Laser-Accelerated Proton Beams as Diagnostics for Cultural Heritage. *Sci. Rep.* **7**, 40415 (2017).
21. Torrisi, L. et al. An unconventional ion implantation method for producing Au and Si nanostructures using intense laser-generated plasmas. *Plasma Phys. Controll. Fusion* **58**, 025011 (2016).

22. Nakamura, K. et al. Diagnostics, control and performance parameters for the BELLA high repetition rate petawatt class laser. *IEEE J. Quantum Electr.* **53**, 1 (2017).
23. Steinke, S. et al. Acceleration of high charge ion beams with achromatic divergence by petawatt laser pulses. *Phys. Rev. Accelerat. Beams* **23**, 021302 (2020).
24. Bin, J. H. et al. Absolute calibration of GafChromic film for very high flux laser driven ion beams. *Rev. Sci. Instrum.* **90**, 053301 (2019).
25. Wilks, S. C. et al. Energetic proton generation in ultra-intense laser–solid interactions. *Phys. Plasmas* **8**, 542 (2001).
26. Fuchs, J. et al. Spatial uniformity of laser-accelerated ultrahigh-current MeV electron propagation in metals and insulators. *Phys. Rev. Lett.* **91**, 255002 (2003).
27. Hegelich, M. et al. MeV ion jets from short-pulse-laser interaction with thin foils. *Phys. Rev. Lett.* **89**, 085002 (2002).
28. E. A. G. Laboratories. *EAG Laboratories* https://www.eag.com/ (2016).
29. Ziegler, J. F., Ziegler, M. D. & Biersack, J. P. SRIM – The stopping and range of ions in matter (2010). *Nuclear Instr. Methods Phys. Res. Section B: Beam Interact. Mater. Atoms* **268**, 1818–1823 (2010).
30. Krása, J. et al. Temperature and centre-of-mass energy of ions emitted by laser-produced polyethylene plasma. *Plasma Phys. Control. Fusion* **49**, 1649 (2007).
31. Shen, J. et al. Fracture analysis of surface exfoliation on single crystal silicon irradiated by intense pulsed ion beam. *Nucl. Instrum. Methods Phys. Res. B* **413**, 6 (2017).
32. Wang, Y. & Nastasi, M. Handbook of Modern Ion Beam Materials Analysis. (Materials Research Society, 2010).
33. Monflier, R. et al. Investigation of oxygen penetration during UV nanosecond laser annealing of silicon at high energy densities. *Appl/ Surf. Sci.* **546**, 149071 (2021).
34. Bustarret, E. et al. Superconductivity in doped cubic silicon. *Nature* **444**, 465 (2006).
35. Feldman, L. C. & Rodgers, J. W. Depth profiles of the lattice disorder resulting from ion bombardment of silicon single crystals. *J. Appl. Phys.* **41**, 3776 (1970).
36. Berhanuddin, D. D. et al. Structural analysis of silicon co-implanted with carbon and high energy proton for the formation of the lasing G-centre. *J. Appl. Phys.* **112**, 103110 (2012).
37. Schenkel, T. et al. Exploration of Defect Dynamics and Color Center Qubit Synthesis with Pulsed Ion Beams. *Quantum Beam Science* **6**, 13 (2022).
38. Song, L. W., Zhan, X. D., Benson, B. W. & Watkins, G. D. Bistable interstitial-carbon–substitutional-carbon pair in silicon. *Phys. Rev. B* **42**, 5765–5783 (1990).
39. Docaj, A. & Estreicher, S. K. Three carbon pairs in Si. *Physica B: Condens. Matt.* **407**, 2981–2984 (2012).
40. Timerkaeva, D., Attaccalite, C., Brenet, G., Caliste, D. & Pochet, P. Structural, electronic, and optical properties of the C-C complex in bulk silicon from first principles. *J. Appl. Phys.* **123**, 161421 (2018).
41. Wang, H., Chroneos, A., Londos, C. A., Sgourou, E. N. & Schwingenschlögl, U. G-centers in irradiated silicon revisited: A screened hybrid density functional theory approach. *J. Appl. Phys.* **115**, 183509 (2014).
42. Richie, D. A. et al. Complexity of small silicon self-interstitial defects. *Phys. Rev. Lett.* **92**, 045501 (2004).
43. Carvalho, A., Jones, R., Coutinho, J. & Briddon, P. R. Density-functional study of small interstitial clusters in Si: Comparison with experiments. *Phys. Rev. B Condens. Matter Mater. Phys.* **72**, 155208 (2005).
44. Santos, I., Aboy, M., López, P., Marqués, L. A. & Pelaz, L. Insights on the atomistic origin of X and W photoluminescence lines inc-Si from ab initio simulations. *J. Phys. D Appl. Phys.* **49**, 075109 (2016).
45. Moussa, J. E. & Cohen, M. L. Constraints onTcfor superconductivity in heavily boron-doped diamond. *Phys. Rev. B* **77**, 064518 (2008).
46. Shen, J. et al. Surface exfoliation analysis on single-crystal silicon under compressed plasma flow action. *Laser Part. Beams* **36**, 129 (2018).
47. Vepsäläinen, A. P. et al. Impact of ionizing radiation on superconducting qubit coherence. *Nature* **584**, 551 (2020).
48. Martinis, J. M. Saving superconducting quantum processors from decay and correlated errors generated by gamma and cosmic rays. *NPJ Quantum Inform.* **7**, 90 (2021).
49. Shaw, B. H., Steinke, S., van Tilborg, J. & Leemans, W. P. Reflectance characterization of tape-based plasma mirrors. *Phys. Plasmas* **23**, 063118 (2016).
50. Kresse, G. & Hafner, J. Ab initiomolecular dynamics for liquid metals. *Phys. Rev. B* **47**, 558 (1993).
51. Kresse, G. & Hafner, J. Ab initio molecular-dynamics simulation of the liquid-metal-amorphous-semiconductor transition in germanium. *Phys. Rev. B Condens. Matter* **49**, 14251 (1994).
52. Kresse, G. & Furthmüller, J. Efficiency of ab-initio total energy calculations for metals and semiconductors using a plane-wave basis set. *Comput. Mater. Sci.* **6**, 15 (1996).
53. Kresse, G. & Furthmüller, J. Efficient iterative schemes for ab initio total-energy calculations using a plane-wave basis set. *Phys. Rev. B Condens. Matter* **54**, 11169 (1996).
54. Krukau, A. V., Vydrov, O. A., Izmaylov, A. F. & Scuseria, G. E. Influence of the exchange screening parameter on the performance of screened hybrid functionals. *J. Chem. Phys.* **125**, 224106 (2006).
55. Andersen, H. C. Molecular dynamics simulations at constant pressure and/or temperature. *J. Chem. Phys.* **72**, 2384 (1980).
56. Perdew, J. P., Burke, K. & Ernzerhof, M. Generalized Gradient Approximation Made Simple. *Phys. Rev. Lett.* **77**, 3865 (1996).

Author contributions
W.R. conducted low-temperature PL measurements; A.J.A., P.A.S., A.P. and B.W. conducted ion pulse and energy deposition analysis; F.I.A. conducted HIM measurements; I.P. conducted SEM measurements; TS conducted optical microscopy; L.O.H., K.N., S.S., J.B., Q.J., A.G., L.G. and T.S. conducted laser ion acceleration experiments; S.B. and C.S. provided theoretical support on laser-ion acceleration; J.G.L. and J.F.F. conducted NRA measurements; H.H. and L.F. conducted ch-RBS measurements; L.Z.T., J.S. and V.I. conducted DFT calculations; R.W., G.B. and J.M. provided early support on color center data acquisition and interpretation; B.K., C.G., C.S., E.E. and T.S. provided supervisory support. All authors contributed to data analysis and the writing of the manuscript.

Competing interests
The authors declare no competing interests.

Additional information